Volume 18, Number 5, 2025. pp. 583-595

Jordan Journal of Physics

ARTICLE

Resonance Frequency Correlation with Negative Refractive Index and Impedance in SRR Structures

Lamyaa A. Jasim[a] and **Hassan A. Yasser**[b]

[a] *Physics Department, Education College, Thi-Qar University, Thi-Qar, Iraq.*

[b] *Physics Department, Science College, Thi-Qar University, Thi-Qar, Iraq.*

Doi: **https://doi.org/10.47011/18.5.3**

Received on: 01/04/2024; *Accepted on: 28/01/2025*

Abstract: This paper underlines the need to improve SRR cell design parameters to achieve both a negative refractive index and optimal impedance matching for advanced metamaterial applications. Metamaterials have unique light manipulation characteristics because of their negative refractive index and excellent impedance matching. This paper looks at numerous split-ring resonator (SRR) cell designs to find the best combinations. Square SRR cells consistently achieved a negative refractive index and excellent impedance matching throughout simulations, outperforming alternative forms such as circular SRRs. Increasing strip width often improves the negative refractive index, although it may create dispersion. Optimal separation distance resulted in a negative refractive index and perfect impedance for particular SRR forms (SSRR, HSRR, and OSRR); however, CSRR designs degraded with greater separations. All SRR forms produced satisfactory results, however CSRR designs had a somewhat poorer performance. Notably, a greater outer side (a = 22mm) SSSR cells resulted in a much higher negative refractive index throughout varying strip widths and separation distances.

Keywords: SRR structures, Resonance frequency correlation, Negative refractive index.

1. Introduction

In the world of electromagnetic engineering, split voltage engineering, known as split ring resonator (SRR), has been truly revolutionary, achieving an unprecedented transformation in our understanding of electromagnetic materials, opening up amazing new opportunities for designing cutting-edge technical systems and devices [1, 2]. Major contributions to metamaterials research were made by R. Shelby *et al.*, who empirically established the existence of a negative refractive index [3]. This pioneering accomplishment set the path for future research into the fundamental principles driving metamaterial behavior, notably SRR structures. Concurrently, theoretical investigations to explicate the function of bianisotropy in producing negative permeability, creating the theoretical framework for comprehending the complexities of SRR-based metamaterials, were conducted by R. Marqués *et al.* [4]. The search to understand the resonance frequency association with negative refractive index in SRR structures has resulted in novel metamaterial characterization techniques [5]. J. Pendry *et al.* introduced a method for determining the effective permittivity and permeability of metamaterials using reflection and transmission coefficients, offering valuable insights into the design and optimization of SRR topologies [6]. Theoretical frameworks that permitted the research of typical electromagnetic phenomena, resulting in the realization of negative refractive index metamaterials, are presented in J. Pendry *et al.* [6]. Furthermore, comprehensive works have served as invaluable resources, providing in-depth analyses of metamaterial physics and engineering explorations that cover the fundamental principles and practical applications of SRR structures [7, 8].

Corresponding Author: Lamyaa A. Jasim **Email**: lamyaa.jasim@utq.edu.iq

Achieving a negative refractive index is the major objective of SRR development. This unusual trait occurs when both the effective permittivity and permeability of the SRR structure become negative at the same time [9, 10]. However, a hidden player, effective impedance, has a substantial impact on performance. Perfect power transmission requires a real part of effective impedance equal to z_0 (the characteristic impedance of open space), which is seldom achieved. In SRRs with a negative refractive index, the imaginary part of the effective impedance frequently differs from zero [11, 12]. This non-zero impedance imaginary part, together with the corresponding real part, adds to energy losses within the SRR, reducing its efficacy. Careful optimization of SRR shape and materials is required to achieve a compromise between obtaining a negative refractive index and reducing energy losses [13]. Researchers can tune the structure's electromagnetic response by precisely altering the size, shape, and composition of the SRR unit cells [14]. This enables them to attain the necessary negative refractive index while reducing the energy losses indicated by the non-zero imaginary element of impedance [15, 16]. The tricky balancing act of getting a negative n while avoiding energy losses is an ongoing focus of research in SRR development. Advances in material science and nanofabrication techniques are paving the way for the development of SRRs with higher performance and lower energy losses [17]. This offers great potential for the creation of new gadgets and applications that take advantage of the unique qualities of negative refraction [18]. Impedance matching is vital in electromagnetic systems to minimize wave reflection and maximize transmission. In metamaterials, particularly those using split-ring resonators (SRRs), it ensures efficient energy transfer and optimal functionality, such as negative refractive indices and enhanced resonance [19]. Proper SRR design aligns impedance with the surrounding medium, reducing energy loss and improving performance in applications like medical imaging, communication systems, and advanced optical devices [20]. This makes impedance matching a cornerstone in SRR-based metamaterial design, enabling broader and more efficient applications [21].

This paper presents a finite element method (FEM)–based simulation study of several SRR unit cell configurations within the COMSOL environment. Also, it focuses on the impedance imaginary part that accompanies this phenomenon and the possibility of achieving an ideal impedance matching, which is a necessary condition in electromagnetic systems.

2. Design of Split Ring Resonators

After conducting simulations in the COMSOL environment, the study aimed to investigate the influence of geometric dimensions and dielectric constants on the bandwidth and resonant frequency of SRRs within the frequency range of 2-6 GHz, essential for modern communication systems. To achieve this, appropriate designs for SRRs were implemented, and a mesh that provided an appropriate balance between result quality and implementation speed was chosen. By altering the shape, number, and dimensions of the rings, specific resonant frequencies with desired bandwidths could be achieved, potentially leading to multiple resonant frequencies within the same frequency range. Four main types of SRR cells were analyzed: square (SSRR), hexagonal (HSRR), octagonal (OSRR), and circular (CSRR). Each SRR cell consists of two metal strips on an insulating surface with a dielectric constant ε_r and thickness h, in the form of two concentric rings, each ring with a width C and separated by a distance D; each ring has a gap of width g, with the gaps oriented in opposite directions. In our work, these rings were in the form of a square, hexagon, octagon, or circle. The length of the dielectric side is L, the distance from the center to the outer edge of the shape is r_{ext} (which is the outer radius of the large ring in the case of CSRR). The background of all the rings is the same: five rectangular strips with width w, length ℓ, and the distance between the strips s. Figure 1 illustrates the model structure in the COMSOL environment.

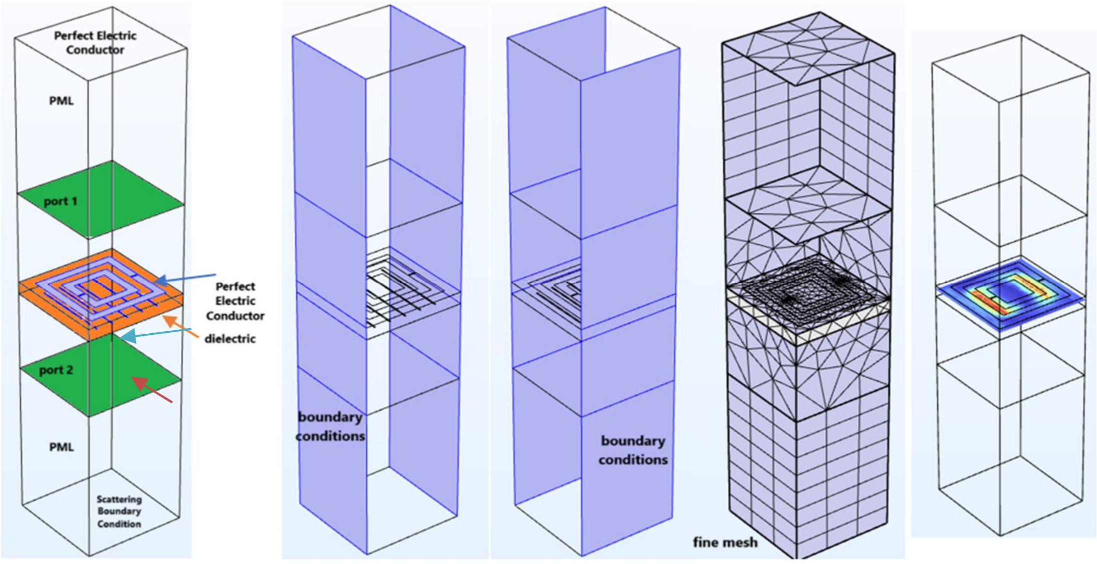

FIG. 1. Structure, ports, PML, periodic conditions, and mesh in COMSOL.

Figure 2 shows the structure of the SSRR unit cell. The rest of the cells differ only in geometric shape and employ the same notation for the engineering parameters. The figure also presents the background structure. The dimensions of the metallic strips, gap width, the distance between strips, dielectric thickness, dielectric constant, the distance between strips in the background, strip width in the background, strip length in the background, cell width, the outer side length, and the outer ring radius are listed in Table 1 for all SRRs, with any changes noted accordingly during the study. Figure 3 shows the convergence test.

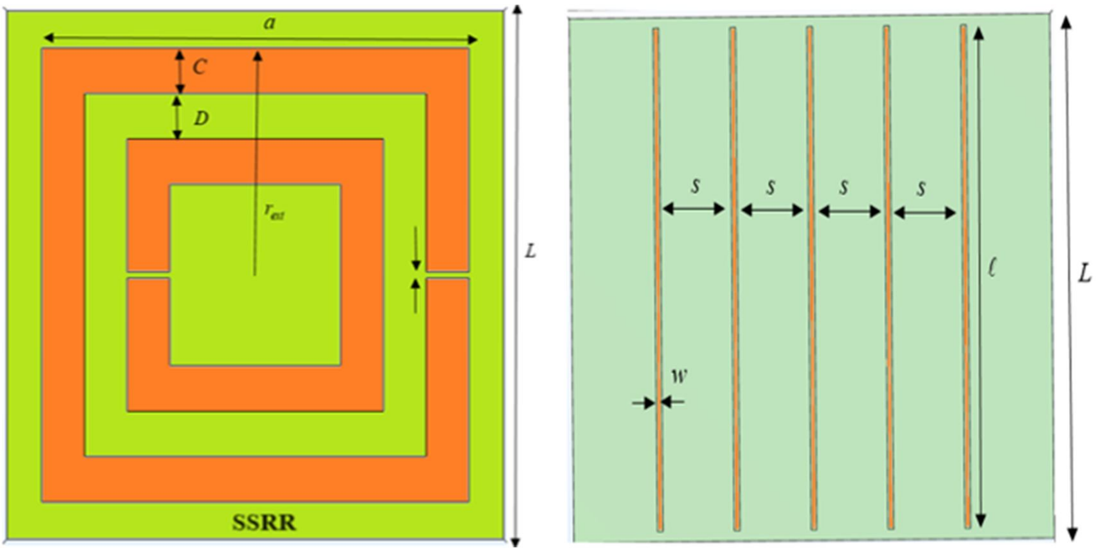

FIG. 2. SSRR structure and background.

TABLE 1. Simulation parameters.

Parameter	SSRR	HSRR	OSRR	CSRR
L	24mm	24mm	24mm	24mm
a	22mm	13.856mm	9.941mm	-
C	2mm	2mm	2mm	2mm
D	2mm	2mm	2mm	2mm
g	0.3mm	0.3mm	0.3mm	0.3mm
r_{ext}	11mm	12mm	11mm	11mm
h	2mm	2mm	2mm	2mm
s	4mm	4mm	4mm	4mm
w	0.3mm	0.3mm	0.3mm	0.3mm

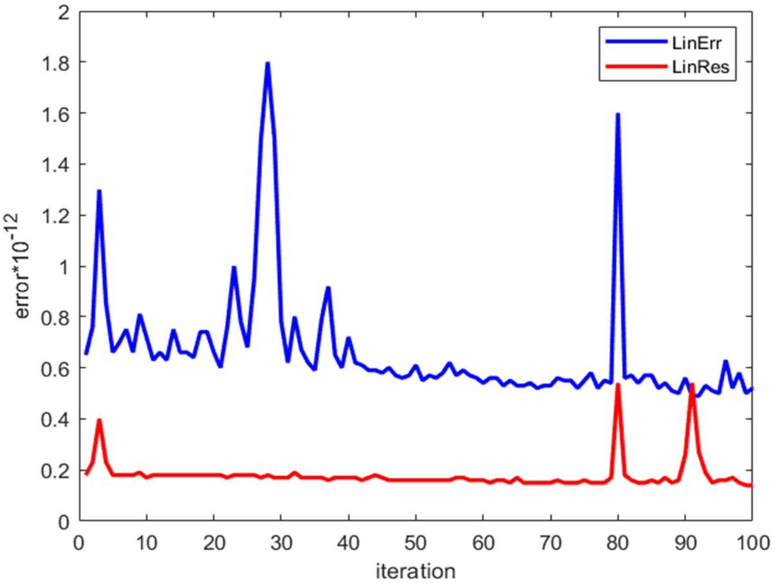

FIG. 3. Convergence test.

3. Retrieval Method Formation

Excitation of SRR with an external magnetic field causes the current to flow from one ring structure to another through the slot between them. As a result, this structure has a very strong displacement current flow. The slots in SRR behave like distributed capacitance, and it behaves like an *LC* circuit. In technical terms, metallic ring structures are modelled by inductance *L* and capacitance *C*. The structure behaves like an *LC* circuit having a resonant frequency given below as [22]:

$$w_R = \frac{1}{\sqrt{L_T C_T}} \qquad (1)$$

where L_T is the total inductance and $C_T$is the total capacitance of the *LC* circuit. The effective parameters of a metamaterial slab are determined by the free-space reflection and transmission coefficients. To determine the parameters at *N* different frequency points, one can either measure the complicated S-parameters or employ full-wave electromagnetic simulators. For normal incident plane waves on a homogeneous metamaterial slab, the relation between the S-parameters, the complex impedance, and the complex refractive index is provided by [23]:

$$S_{11} = \frac{\Gamma(1-e^{-2in_{eff}kt})}{1-\Gamma^2 e^{-2in_{eff}kt}} \qquad (2)$$

$$S_{21} = \frac{(1-\Gamma^2)e^{-in_{eff}kt}}{1-\Gamma^2 e^{-2in_{eff}kt}} \qquad (3)$$

where $\Gamma = (z_{eff}-1)/(z_{eff}+1)$, t is the metamaterial slab thickness, and n_{eff} is the complex effective refractive index ($n_{eff} = n' + in''$), with $n'$and n' being the real and imaginary parts of n_{eff}, respectively. The parameters S_{11} and S_{21} are complex and related to reflectance and the transmittance, respectively, as: $r = |S_{11}|^2$ and $t = |S_{21}|^2$.

The complex effective wave impedance z_{eff} is defined as [24]:

$$z_{eff} = R + iX = R + i\left(wL_T - \frac{1}{wC_T}\right) \qquad (4)$$

The parameters z_{eff}, n_{eff} are related to S-parameters as [22]:

$$z_{eff} = \pm\sqrt{\frac{(1+S_{11})^2 - S_{21}^2}{(1-S_{11})^2 - S_{21}^2}} \qquad (5)$$

$$n_{eff} = \pm\frac{1}{k_o a}\cos^{-1}\left(\frac{1-S_{11}^2+S_{21}^2}{2S_{21}}\right) + \frac{2\pi m}{k_o a}, m = 0,1,2\ldots \qquad (6)$$

where k_o is the free-space wavenumber, m is the multivalued logarithmic function's branch index, and a is the metamaterial slab thickness. As seen in [25], when the metamaterial thickness is modest, m is set to zero. When a is large, these branches can lie arbitrarily close to one another, making the selection of the correct branch difficult in the case of dispersive materials. For this reason, the best results are obtained for the smallest possible thickness of the sample, as is commonly known in the analysis of continuous materials. Even with a small sample, more than one thickness must be measured to identify the correct branches of the solution that yield consistently the same values for n.

The real value of the complex wave impedance and the imaginary value of the complex refractive index must both be greater than or equal to zero for a passive metamaterial, i.e., $R \geq 0, n'' \geq 0$. Therefore, the sign of z_{eff} must be decided in light of those circumstances. Specifically, the real and imaginary components of the complex refractive index are $n' = Re\{n_{eff}\}$, $n'' = Im\{n_{eff}\}$, respectively [26]. There are ambiguities in the formulations of the metamaterial's effective permittivity and permeability due to the resultant branch uncertainty in the real part of the complex refractive index. The following formulas connect the complex permittivity and complex permeability to the complex refractive index and the wave impedance [27]:

$$\varepsilon_{eff} = n_{eff}/z_{eff} \qquad (7)$$

$$\mu_{eff} = n_{eff} z_{eff} \qquad (8)$$

4. Results and Discussion

Figure 4 depicts the relationship of S_{11} with frequency in the 2-6 GHz band using various values of D, which denote the distance between two strips. It is worth noting that each D value results in various behaviors in terms of resonance frequency, bandwidth, and minimum attainable value. While it is possible to achieve another resonant frequency within the same range, our attention is on the case with a greater bandwidth, also known as the fundamental resonant frequency. Furthermore, when D grows, the fundamental resonant frequency shifts to the right. However, it is critical to understand that D cannot expand indefinitely since it is inextricably tied to cell size.

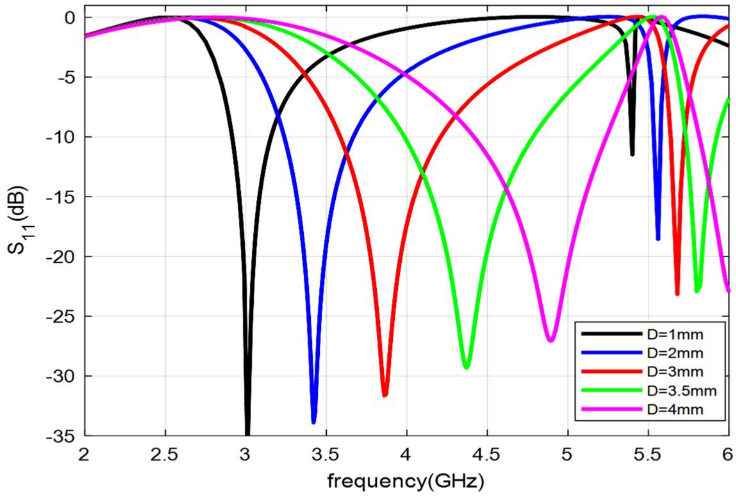

FIG. 4. S_{11} as functions of frequency using many values of D for SSRR.

In Fig. 5, we show the connection between the normalized real refractive index and the normalized frequency for various C values inside the SSRR cell. Our primary focus is on the fundamental resonance frequency, which demonstrates a clear relationship between the refractive index and resonance frequency regions. Although comparable patterns appear when additional parameters such as C, s, h, a, and dielectric constant are changed, it is worth noting that the resonant frequency and bandwidth vary with time. As a result, we avoid demonstrating these recurrent actions. Instead, we stress the resonance frequency's relationship with the negative refractive index, as well as the real and imaginary parts of impedance.

Figure 6 presents the real part of the refractive index, the imaginary part of the impedance, and the real part of impedance at resonance as functions of strip width for many SRRs at $h = 3$ *mm*, $D = 2$ *mm*, $\varepsilon_r = 4.3$, $s = 4$ *mm*. Figure 6(a) shows that the resonance frequency occurs when the refractive index is negative. In general, raising C leads to an increase in the real refractive index. The CSRR cell exhibits the highest real refractive index, while the SSRR shows the lowest. The figure shows that the real refractive index is negative until it approaches $C > 3$, after which it is positive in the case of cell CSRR. However, it always remains negative in SSRR and OSRR cells. When C is less than 3.5, the HSRR cell produces a negative refractive index. The metamaterial property is attained for all cells by creating $C < 3$. It is clearly evident from Fig. 6(b) that the imaginary part of the impedance is close to zero at first and then increases slowly as the strip width increases for square, hexagonal, and octagonal cells, but it increases strongly in the case of the circular cell and then decreases to negative values. Losses and imperfect coupling between the cell and wire may increase the imaginary value of impedance. Additionally, nonlinear effects can introduce extra frequency components into the cell response, further causing deviations of the impedance imaginary part from zero. In general, increasing the strip width makes the impedance imaginary part non-zero.

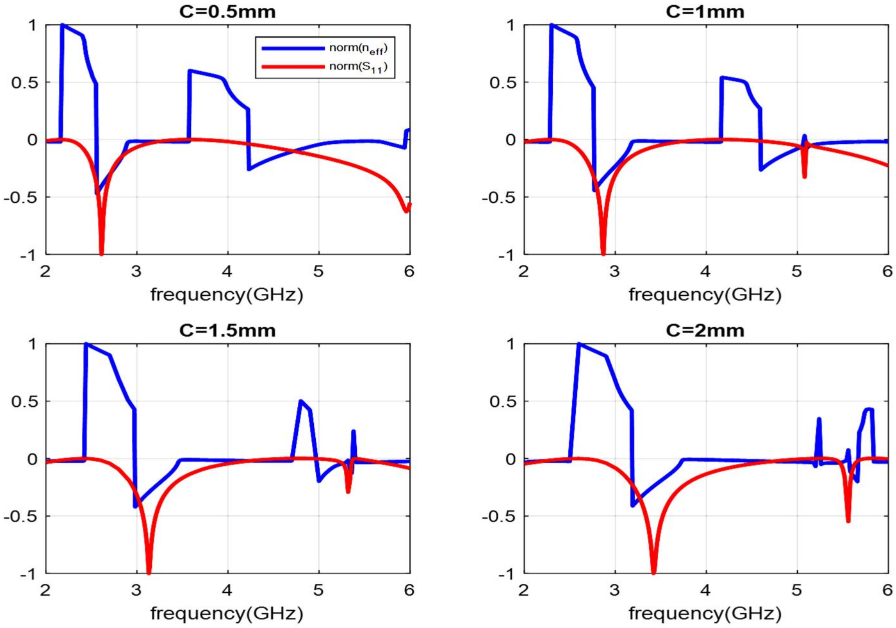

FIG. 5. Normalized S_{11} and effective refractive index as functions of frequency using many values of strip width for SSRR.

In Fig. 6(c), the matching between the system impedance and the characteristic impedance happens at $z_{eff}/z_0 = 1$. When condition $z_{eff}/z_0 = 1$ is met, the ideal case for electromagnetic systems occurs. Note that condition $z_{eff}/z_0 = 1$ is achieved almost at the beginning for all cells, but it is not achieved as *C* continues to increase, and the cell furthest from condition $z_{eff}/z_0 = 1$ is the CSRR cell. The cases $z_{eff}/z_0 > 1$ indicate that the SRR cell's effective impedance exceeds the line's characteristic impedance. The entering electromagnetic wave may be reflected at the SRR cell interface due to an impedance mismatch. The greater the ratio z_{eff}/z_0, the stronger the reflection may be. When $z_{eff}/z_0 < 1$, the SRR cell's effective impedance is lower than the line's characteristic impedance. In this situation, the SRR cell may cause dispersion, which means that the propagation speed of different frequencies within the electromagnetic wave will vary. The smaller the ratio z_{eff}/z_0, the greater the dispersion impact may be.

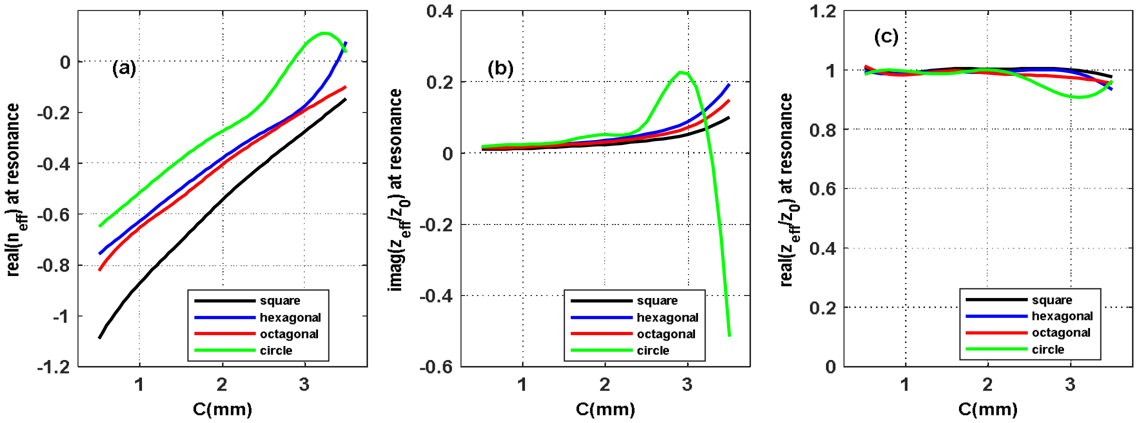

FIG. 6. Real part of the refractive index, imaginary part of the impedance, and real part of the impedance at the resonance frequency as functions of strip width for many SRRs.

Figure 7 shows the dependence of the real part of the refractive index, the imaginary part of the impedance, and the real part of impedance at resonance on the distance between the strips for many SRRs at h = 3 *mm*, C = 2 *mm*, $\varepsilon_r = 4.3$, and s = 4 *mm*. Figure 7(a) shows that the real part of the refractive index is negative at the resonance frequency when D < 4.7 *mm* for square, HSRR, and OSRR cells, and it is negative in the case of the CSRR cell when D < 3.8 *mm*. Note that the SSRR/CSRR cells always represent the lowest/highest real refractive index. Figure 7(b) shows that the imaginary part of the impedance starts close to zero for all cells except the CSRR case, and after D > 3.5 *mm,* the values begin to increase or decrease depending on the cell type, with HSRR and OSRR cells maintaining some degree of stability until D = 3.5 *mm*. In the case of the CSRR cell, the impedance imaginary part is not the same as its predecessors but rather alternates between positive and negative. Also, the SSRR cell will have values far from zero when D = 3 *mm*. In general, the negative imaginary part of the impedance moves away from zero in response to the corresponding negative refractive index. Positive values mean that the characteristic of inductance is dominant, and negative values mean that the characteristic of capacitance is dominant, while a zero value means that the impedance is composed of resistance only. Figure 7(c) shows that the condition $z_{eff}/z_0 = 1$ is met for HSRR and OSRR cells at D < 3.8 *mm*, while it is met at D < 3 *mm* for SSRR cells. In the case of the CSRR cell, the impedance varies greatly, and condition $z_{eff}/z_0 = 1$ is not met except at a few points. In general, for all cells except the CSRR cell, a wide range of D values can be obtained that achieve a negative refractive index, zero impedance imaginary part, and meet the necessary condition $z_{eff}/z_0 = 1$ for the ideal case in electromagnetic systems.

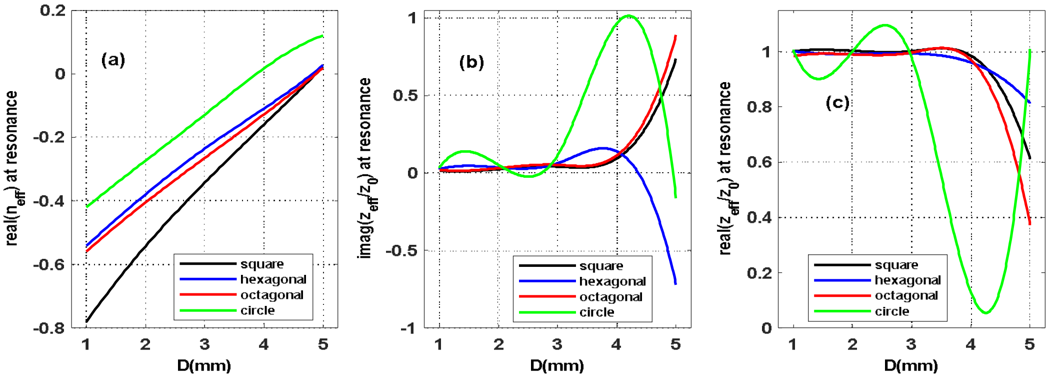

FIG. 7. Real part of the refractive index, imaginary part of the impedance, and real part of the impedance at the resonance frequency as a function of distance between the strips for many SRRs.

Figure 8 shows the dependence of the real part of the refractive index, the imaginary part of the impedance, and the real part of impedance at resonance on the dielectric thickness for many SRRs at D = 2 *mm*, C = 2 *mm*, $\varepsilon_r = 4.3$, s = 4 *mm*. Figure 8(a) shows that a negative refractive index is achieved in HSRR and CSRR cells as long as h < 2.3 *mm*. It is achieved for SSRR and OSRR cells as long as h < 2.8 *mm*. The SSRR/CSRR cells achieve the lowest/highest negative refractive index. Figure 8(b) shows a slight increase in the impedance imaginary part values for all cells, with the impedance imaginary part of the CSRR/SSRR cells being the highest/lowest. We can confirm here that the impedance imaginary part is small under the simulated conditions. Also, we note that the impedance imaginary part corresponding to negative refractive indices is the lowest. Note that the imaginary part of impedance should be zero at the resonant frequency, but this was not achieved due to neglecting the phenomena of loss, coupling, and nonlinearity. This is due to the following: at the resonance frequency $z_{eff} = z_0$, the effective impedance will be real, and the imaginary impedance will be zero; and due to absorption effects, coupling within the cell parts, and perhaps also nonlinear effects that can occur in the insulator, the imaginary part of the impedance will not be zero at the resonance frequency.

Figure 8(c) shows the fulfillment of the condition $z_{eff}/z_0 \approx 1$, which is necessary for electromagnetic systems for all values of h using every SRR cell. The sign of approximation, not equality, is used due to the presence of a small amount of impedance imaginary part, depending on the cell type.

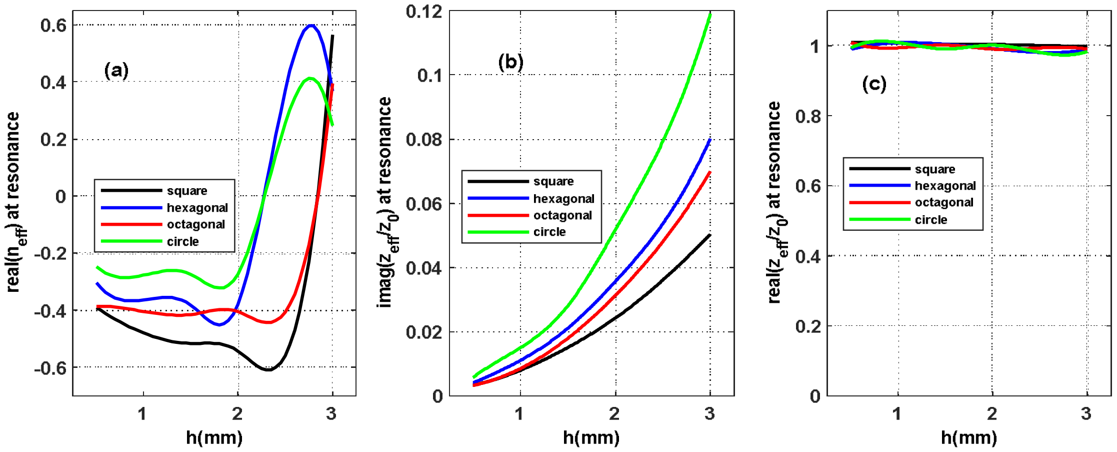

FIG. 8. Real part of the refractive index, imaginary part of the impedance, and real part of the impedance at resonance frequency as a function of dielectric thickness for many SRRs.

Figure 9 shows the dependence of the real part of the refractive index, the imaginary part of the impedance, and the real part of the impedance at resonance on the dielectric thickness for many SRRs at D = 2 mm, C = 2 mm, $\varepsilon_r = 4.3$, h = 3 mm. Figure 9(a) shows that a negative refractive index is achieved at all values of s and for all cells, with SSRR/CSRR cells achieving the lowest/highest negative refractive indices. It can also be noted that the variation of the refractive index in all cases is small. The figure shows that the impedance imaginary part in all cells has small values and that SSRR/CSRR achieves the lowest/highest values, and the impedance imaginary part in the case of the CSRR cell is three or four times greater than that of the SSRR cell. In general, it can be understood from this that the conditions causing negative impedance (losses, coupling, and nonlinearity) are minimal under the simulated conditions. Figure 9(c) shows that condition $z_{eff}/z_0 \approx 1$ is met at the resonance frequency for all values of s and for all cells used. Accordingly, under the present simulation conditions, a metamaterial with a near-zero impedance imaginary part can be obtained, and the ideal impedance condition can be achieved.

Figure 10 shows the dependence of the real part of the refractive index, the imaginary part of the impedance, and the real part of the impedance at resonance on the dielectric constant value for SSRR and CSRR cells at D = 2 mm, C = 2 mm, s = 4 mm, h = 3 mm. Figure 10(a) shows that SSRR/CSRR achieve the lowest/highest negative refractive indices over every dielectric constant range. In Fig. 10(b), the impedance imaginary part achieved in the case of CSRR is much larger than in SSRR, but in general, it is very small. Figure 10(c) demonstrates that near-ideal impedance matching is maintained across all dielectric constant values for the two cells used. The current simulation conditions achieved the metamaterial property, reduced the impedance imaginary part to the lowest possible level, and achieved the ideal impedance condition.

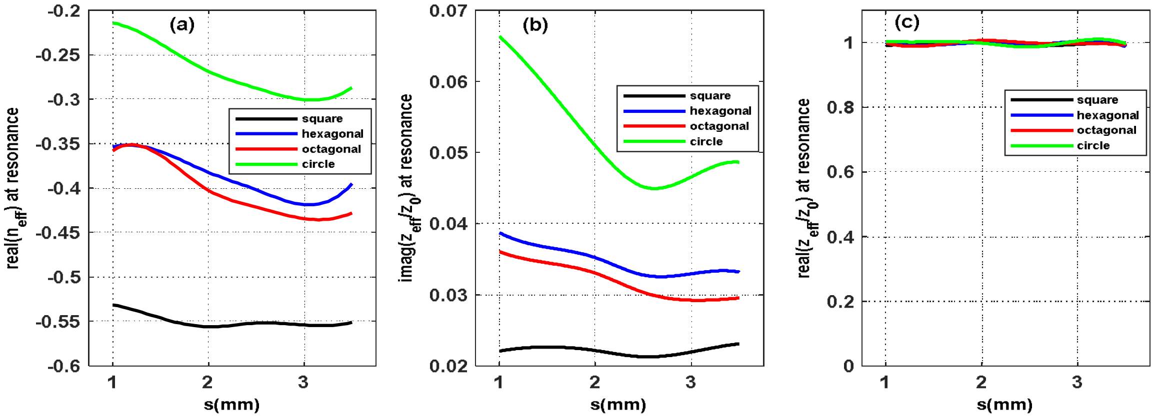

FIG. 9. Real part of the refractive index, imaginary part of the impedance, and real part of the impedance at resonance frequency as a function of distance between strips in the background for many SRRs.

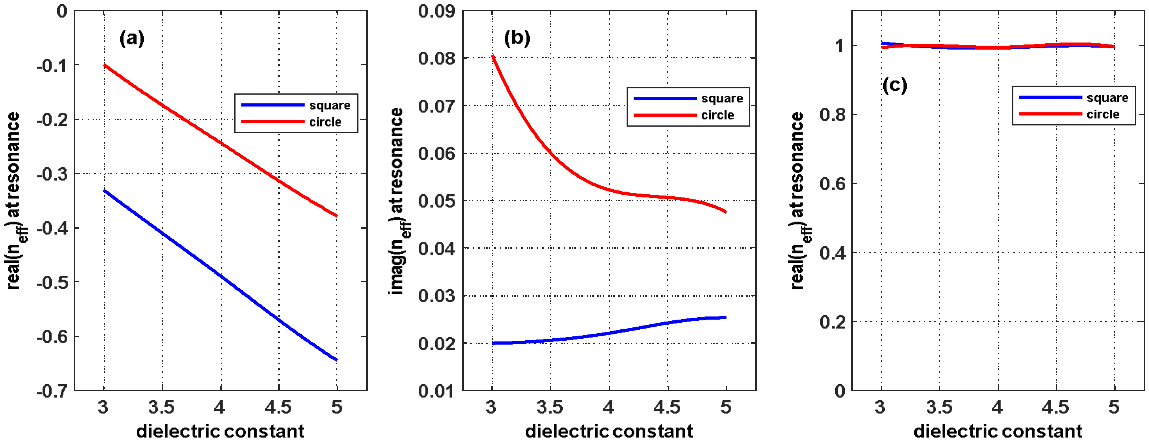

FIG. 10. Real part of the refractive index, imaginary part of the impedance, and real part of the impedance at the resonance frequency as a function of dielectric constant for SSRR and CSRR cells.

Figure 11 shows the dependence of the real part of the refractive index, the imaginary part of the impedance, and the real part of impedance at resonance on strip width for SSRR (a = 22 mm, a = 20 mm) and CSRR ($r_{ext} = 11\,mm, r_{ext} = 10\,mm$) cells at D = 2 mm, s = 4 mm, h = 2 mm, $\varepsilon_r = 4.3$. Figure 11(a) shows that the SSRR cell (a = 22 mm) exhibits the lowest negative refractive index for all strip widths. The SSRR (a = 20 mm) and CSRR ($r_{ext} = 11\,mm$) cells have a negative refractive index up to a strip width C < 2.9 mm. The CSRR ($r_{ext} = 10\,mm$) cell has the largest negative refractive index up to strip width C < 2.3 mm. Figure 11(b) shows an impedance imaginary part that increases slightly with the increase in the strip width of the SSRR cell (a = 22 mm). For the SSRR (a = 22 mm) and CSRR($r_{ext} = 11\,mm$) cells, the impedance imaginary part starts small, then increases slightly, and then increases strongly and decreases to negative values. For the CSRR cell ($r_{ext} = 10\,mm$), we see that the impedance imaginary part changes severely, which is the worst case. This means that the nature of the impedance imaginary part depends on the achievement of the negative refractive index. In general, a near-zero imaginary impedance is observed only within a limited range of strip widths.

Figure 11(c) confirms this trend for impedance matching. Ideal impedance condition $z_{eff}/z_0 \approx 1$ is achieved only over a small strip width range for most cells.

For C > 1.5 mm, all cells except the SSRR (a = 22 mm) deviate from the ideal condition. The SSRR cell (a = 22 mm) maintains near-ideal impedance $z_{eff}/z_0 \approx 1$ across the full range of strip widths. Overall, for all cells, near-ideal impedance consistently coincides with a negative refractive index at the resonance frequency.

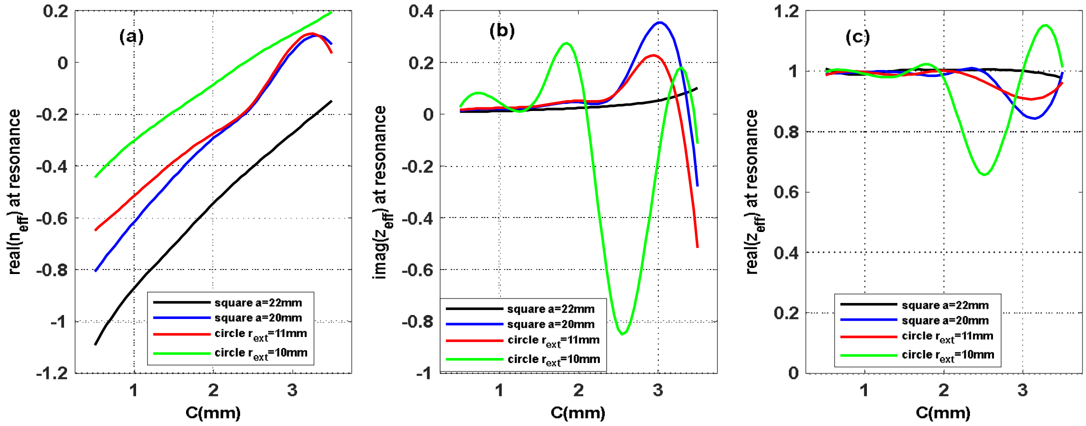

FIG. 11. Real part of the refractive index, imaginary part of the impedance, and real part of the impedance at resonance frequency as a function of strip width for many SRR cells.

Figure 12 shows the dependence of the real part of the refractive index, the imaginary part of the impedance, and the real part of the impedance at resonance on the distance between strips for SSRR (a = 22 mm, a = 20 mm) and CSRR ($r_{ext} = 11\,mm, r_{ext} = 10\,mm$) cells at C

= 2 *mm*, *s* = 4 *mm*, *h* = 2 *mm,* and $\varepsilon_r = 4.3$. Figure 12(c) shows that the SSRR cell (*a* = 22 *mm*) achieves a negative refractive index at *D* < 4.8 *mm*, and that the two cells, SSRR (*a* = 20 mm) and CSRR ($r_{ext} = 11\,mm$), achieve a negative refractive index at *D* < 3.7 *mm*. The CSRR ($r_{ext} = 10\,mm$) cell shows the most irregular behavior, with the refractive index initially negative, then becoming positive, and returning to negative values. Figure 12(b) shows that the SSRR cell (*a* = 22 *mm*) initially achieves near zero impedance imaginary part and then increases, while the other cells exhibit significant variations in the imaginary impedance across the range.

Figure 12(c) shows the impedance matching condition. Near-ideal impedance is achieved only at the beginning for the SSRR cell (*a* = 22 *mm*). All other cells remain far from the ideal impedance condition throughout the examined range.

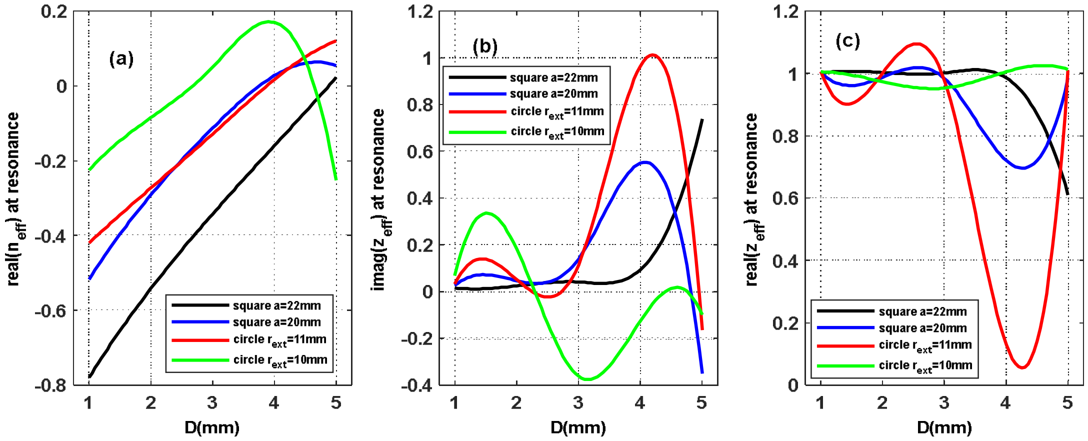

FIG. 12. Real part of the refractive index, imaginary part of the impedance, and real part of the impedance at the resonance frequency as a function of distance between strips for many SRR cells.

Figure 13 shows the bandwidth, resonance frequency, and minimum S_{11} as functions of the dielectric thickness *h* for the four types of SRR.

The bandwidth decreases as *h* increases. The octagonal cell exhibits the smallest bandwidth, while the circular and square cells show similar bandwidth values at *h* = 0.7, 2 mm. The figure representing the resonance frequency as a function of *h* shows that the resonance frequency is inversely proportional to the dielectric thickness. Among the geometries, the circular cell achieves the highest resonance frequency, whereas the square cell exhibits the lowest. The figure that represents the minimum value of S_{11} as a function of h shows a direct proportion between the minimum value of S_{11} and the dielectric thickness. We notice that the minimum value of S_{11} is the highest possible in the case of circuit, but when it is less than *h* = 1 mm, it begins to decline and achieves the lowest value for the minimum value of S_{11} and also in the octagonal state, at less than *h* = 1.5 mm, it begins to decline and is less than the square case.

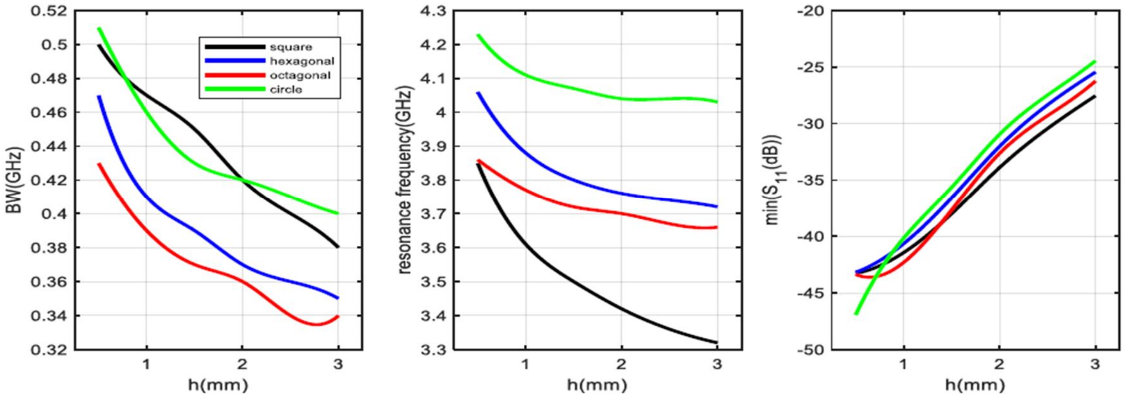

FIG. 13. Bandwidth, resonance frequency, and minimum value of S_{11} as functions of *h* for different SRRs.

Figure 14 shows the bandwidth, resonance frequency, and minimum value of S_{11} as functions of *D* using four types of SRR. It appears from the figure representing the bandwidth as a function of *D* that the bandwidth increases with increasing *D* for all four types of SRR, but for the case of the circuit, we notice that it tends to stabilize from *D* = 4.5 mm and above. The largest bandwidth is obtained for the square, while the octagonal exhibits the smallest. The resonance frequency appears to increase with increasing *D* in the case of a circle and decrease correspondingly in the case of a square. The minimal value of S_{11} appears to increase as *D* increases; however, in the case of an octagonal, the minimum value of S_{11} tends to stabilize between *D* = 1 mm and *D* = 1.5 mm. The peak is the largest in the case of a circle and the least in the case of a square. Figure 15 shows the bandwidth, resonance frequency, and minimum value of S_{11} as functions of *C* for the four types of SRR. The bandwidth increases with increasing *C* for all cases; however, for the circuit, it tends to stabilize for *C* = 2.5 mm and above. The bandwidth is the largest possible in the case of a square and the smallest possible in the case of an octagonal. The resonance frequency increases with increasing *C* in the case of a circle and decreases as much in the case of a square. The minimal value of S_{11} appears to increase as *C* increases; however, in the case of an octagonal, the minimum value of S_{11} tends to stabilize between *C* = 0.5mm and *C* = 1.5mm. The peak is the largest possible in the case of a circle and the least possible in the case of a square. When the strip width in the SRR is increased, reflections and deviations in the signal transmission are reduced, and this is reflected by increasing the minimum value of S_{11}.

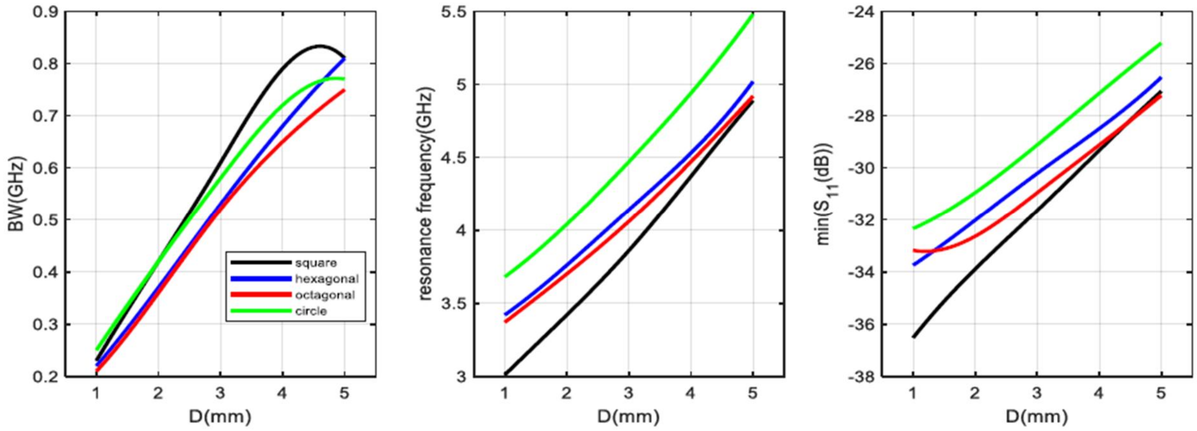

FIG. 14. Bandwidth, resonance frequency, and minimum of S_{11} as functions of *D* for different SRRs.

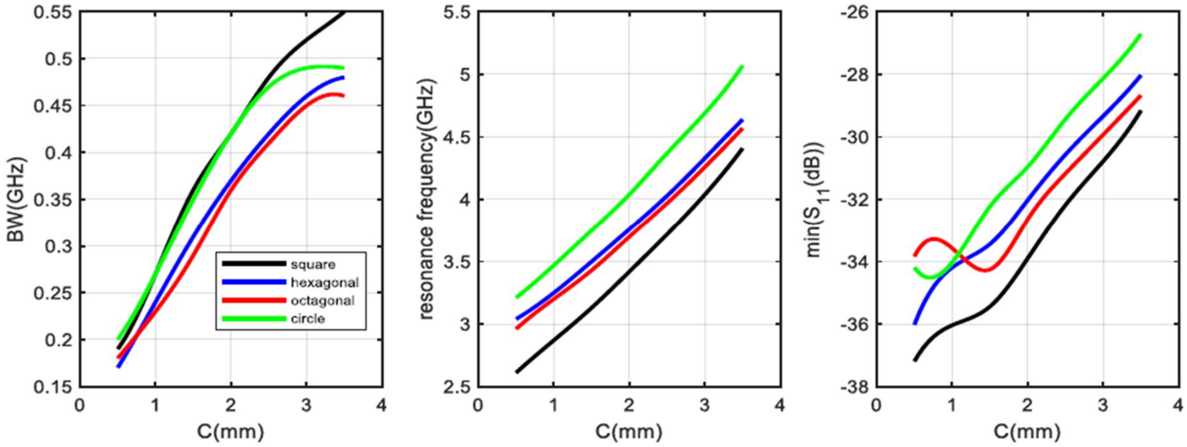

FIG. 15. Bandwidth, resonance frequency, and minimum of S_{11} as functions of *C* for different SRRs.

5. Conclusions

In conclusion, increasing *C*, *D*, and h leads to an increase in the resonant frequency and bandwidth, and, in some cases, to the appearance of additional resonant modes for the four types of SRR. The resonant frequency, the bandwidth, and the minimum value of S_{11} increase with increasing C and D for all types of SRR, and there may be some cases of stability in some types of SRR. The SSRR cell consistently achieved a negative refractive index and excellent impedance matching throughout several simulations. This shows that the metamaterials have strong characteristics, making them suitable designs. Other cell forms, such as CSRR, often fared poorly. Wider strips enhance the negative refractive index but may add undesirable features, such as dispersion. The optimal spacing between strips resulted in a negative refractive index and perfect impedance $z_{eff} \approx z_0$ for SSRR, HSRR, and OSRR cells, whereas CSRR designs suffered at wider separations. For varying strip widths and dielectric constants, all SRR forms obtained a negative refractive index and excellent impedance matching. However, the performance of the CSRR design was marginally lower. Larger side lengths (a = $22mm$) resulted in improved negative refractive index values for both strip width and strip separation changes. The work emphasizes the need to improve SRR cell design characteristics, particularly the outer radius, to achieve both a negative refractive index and optimal impedance matching for metamaterial applications.

References

[1] Tian, S., Zhang, X., Wang, X., Han, J., and Li, L., Nanophotonics, 11 (9) (2022) 1697.

[2] Rhee, J., Kim, Y., Yi, C., Hwang, J., and Lee, Y., J. Electromagn. Waves Appl., 34 (2020) 1338.

[3] Shelby, R., Smith, D., Nemat-Nasser, S., and Schultz, S., Appl. Phys. Lett., 78 (2001) 489.

[4] Marqués, R., Medina, F., and El-Idrissi, R., Phys. Rev. B, 65 (2002) 144440-1.

[5] Smith, D., Schultz, S., Markoš, P., and Soukoulis, C., Phys. Rev. B, 65 (2002) 195104.

[6] Pendry, J., Holden, A., Robbins, D., and Stewart, W., IEEE Trans. Microw. Theory Tech., 47 (1999) 2075.

[7] Eleftheriades, G. and Balmain, K., "Negative Refraction Metamaterials: Fundamental Principles and Applications", 1st Edition, (John Wiley and Sons, Hoboken, 2005).

[8] Engheta, N. and Ziolkowski, R., "Metamaterials: Physics and Engineering Explorations", (IEEE Press, The Institute of Electrical and Electronics Engineers, Inc., 2006).

[9] Esmail, B., Majid, H., Saparudin, F., Jusoh, M., Ashyap, A., Al-Fadhali, N., and Rahim, M., Bull. Electr. Eng. Inform., 9 (3) (2020) 1038.

[10] Kalel, S. and Wang, W., Prog. Electromagn. Res. C, 132 (2023) 159.

[11] Sifat, R., Faruque, M., Ramachandran, T., Abdullah, M. and Al-Mugren, K., Heliyon, 10 (1) (2024).

[12] Qiong Zhang, Z., Cao, W., Gao, M., Liu, Y., and Chu, W., Heliyon, 9 (11) (2023).

[13] Ramachandran, T., Mri, F., Ahamed, E., and Abdullah, S., Results Phys., 15 (2019) 1.

[14] Singh, H., Mittal, N., and Arora, O., Mater. Today, Proc., 33 (3) (2020) 1552.

[15] Singh, H., Sohi, B.S., and Gupta, A., Bull. Mater. Sci., 42 (2019) 1.

[16] Islam, S.S., Rahman, M.A., Faruque, M.R.I., and Islam, M.T., Sci. Eng. Compos. Mater., 25 (1) (2018) 59.

[17] Islam, S.S., Khan, M.S., and Faruque, M.R.I., Mater. Res. Express, 6 (12) (2020).

[18] Shah, A. and Ghalsasi, P., Navrachana Univ. Interdiscip. J., 5 (2) (2022).

[19] Madhavamoorthi, S., Marishwari, M., Kashif, H., Shen, S., Chen, B., Xie, H., Ouyang, Z., and Liu, Q., Opt. Express, 32 (22) (2024) 38422.

[20] Nguyen, Q. and Zaghloul, A., IEEE Int. Symp. Antennas Propag. USNC/URSI Natl. Radio Sci. Meet., Boston, MA, USA, (2018) 439.

[21] Portosi, V., Loconsole, A., and Prudenzano, F., Appl. Sci., 10 (2020) 6740.

[22] Khalili, F. , Honarvar, M. , Moghadasi, M., and Dolatshahi, M., Int. J. RF Microw. Comput.-Aided Eng., 30 (1) (2020) e22006.

[23] Islam, M., Islam, M.T., Moniruzzaman, M., and Muhammad, G., Results Phys., 19 (2020) 103556.

[24] Hossain, Md., Faruque, M., Islam, S., and Islam, M., Sci. Rep., 11 (1) (2021) 19331.

[25] Moniruzzaman, Md., Islam, M., Samsuzzaman, Md., Salaheldeen, M., Sahar, N., Bawri, S., Almalki, S., Alsaif, H., and Islam, Md., Sci. Rep., 12 (1) (2022) 1.

[26] Islam, Md., Islam, M., Soliman, M., Baharuddin, M., Mat, K., Moubark, A., and Almalki, S., Sci. Rep., 11 (2021) 21782.

[27] Aladadi, Y. and Alkanhal, M., Opt. Mater. Express, 9 (9) (2019) 3765.